JOURNAL OF MATERIALS SCIENCE 22 (1987) 2569–2582

Xerographic properties of single- and double-layer photoreceptors based on amorphous selenium–tellurium alloys

C. JUHASZ, M. VAEZI-NEJAD*, S. O. KASAP‡
Solid State Research Group, Department of Electrical Engineering, Imperial College of Science and Technology, University of London, London SW7 2BT, UK

Single- and double-layer xerographic photoreceptors were fabricated by vacuum deposition of a-$Se_{1-x}Te_x$ alloy films on aluminium substrates. Double-layer photoreceptors comprised of a thin (a few micrometres) a-$Se_{1-x}Te_x$ alloy serving as a photogeneration layer (PGL) on a thick (50 to 60 μm) a-Se layer acting as a charge transport layer (TL). Xerographic dark discharge experiments on a-Se films indicated that the decay of the surface potential over the time scale of observation ($\sim$500 sec) is essentially due to bulk thermal generation of holes, and their consequent sweep-out and depletion. Hole emission occurs from discrete midgap localized states and it is field-assisted. When a-Se is alloyed with tellurium the dark discharge becomes more rapid due to an increase in both the volume density and energy spread of the midgap hole emission centres with tellurium concentration. In double-layer photoreceptors, with a tellurium content over 3 wt%, although the PGL was only a few micrometres in thickness, the dark discharge was mainly due to the tellurium-rich PGL. The repetition of the xerographic cycle over many cycles leads to the saturation of the surface residual voltage which was used to determine the concentration N_t of deep hole traps. For a-Se, N_t (1.9×10^{13} cm^{-3}) was found to be comparable to the concentration of midgap hole emission centres, which suggested that amphoteric neutral centres (possibly intimate valence alternation pairs) are involved in hole capture and emission. The saturated residual voltage $V_{r\infty}$ in a-$Se_{1-x}Te_x$ alloy films increased with the tellurium content up to 6 to 8 wt% Te due to tellurium-introduced deep traps. In double layers, the saturated residual voltage was more than that expected from the properties of monolayers, due probably to the presence of deep hole traps at the PGL–TL interface. Xerographic time-of-flight (XTOF) experiments confirmed the previous results from the electroded TOF experiments that tellurium addition increases the density of shallow traps. Combining the TOF data with the saturated residual voltage measurements gives a hole capture coefficient C_t of $\sim 1.2 \times 10^{-8}$ cm^3 sec^{-1} for pure a-Se. Chlorine doping of a-Se resulted in a very rapid dark discharge and a fall in the saturated residual voltage.

1. Introduction

Amorphous $Se_{1-x}Te_x$ alloys with tellurium contents up to $\sim$25 wt% play an important role in the commercial xerographic photoreceptor industry due to their more desirable spectral response in comparison with pure and halogen-doped a-Se and a-$Se_{0.995}As_{0.005}$. Depending on the specific xerographic application the current trend in photoreceptor design is to use single- and multi-layer structures of various compositions of a-Se alloyed with tellurium or arsenic with small amounts of some chlorine in the parts per million range to obtain optimal xerographic performance [1–6]. Alloying with tellurium reduces the bandgap and thus increases the spectral sensitivity towards the red region [5, 7–11] which is essential for laser and LED types of printer applications. Recent developments in the technology of xerographic photoreceptors have been reviewed by a number of authors [1–3].

Although optical [8–11] charge transport [12–16] and thermal ([17] and references therein) properties of a-$Se_{1-x}Te_x$ have received an increased interest over the last few years there has been, however, very limited systematic xerographic characterization of this alloy system. In this work we report on a number of xerographic measurements which are based on an initial corona charging of the photoconductor as in the xerographic cycle. The following measurements were then performed.:

(i) dark discharge;
(ii) xerographic residual and saturated residual voltage;
(iii) xerographic time-of-flight (XTOF).

Dark-discharge meaurements involve monitoring

Present address: School of Electronic Systems Engineering, Kingston Polytechnic, Kingston-upon-Thames, Surrey, UK.
‡*Present address*: Department of Electrical Engineering, University of Saskatchewan, Saskatoon S7N 0W0, Canada.

0022–2461/87 $03.00 + .12

the time dependence of the surface potential on the photoreceptor. There are a number of possible physical processes which lead to the decay of the surface voltage. Experimental results support a bulk generation of free carriers, of the same sign as the surface charge, and their sweep-out which leaves a "depleted" volume of sample with an oppositely charged bulk space charge due to immobile ionic centres. As bulk generation proceeds with time, the surface voltage is reduced by the integral of the electrical field of the bulk ions across the specimen thickness. We must also consider the dark-discharge component due to surface generation and substrate contact injection. The latter become important at the highest charging voltages.

Xerographic residual and saturated residual voltage measurements probe the influence of deep traps on charge transport in the sample. Residual voltage is defined as the surface potential remaining after an intense flash illumination of a charged photoreceptor. It is due to some of the photoinjected carriers becoming deeply trapped during their transit across the sample. If the photoreceptor is repeatedly charged and discharged by strong pulse illumination, the residual voltage builds up with the number of cycles and eventually saturates [18]. The surface voltage is then termed the saturated residual voltage, $V_{r\infty}$, and provides information on the density of deep traps.

The xerographic time-of-flight (XTOF) experiment is essentially identical in principle to the conventional electroded time-of-flight (ETOF) experiment which requires the specimen to be sandwiched between two electrodes. In XTOF the top electrode is eliminated and instead electrostatic charge is deposited on to this surface from a corona device. The technique has been recently described by Xerox workers [19, 20] to expose its powerful analytical applications.

An optimal photoreceptor design will require, amongst many other features, high charge acceptance, slow dark discharge, low first and cycled-up saturated residual voltages and large charge-carrier drift mobilities. Increasing the tellurium content of an a-Se-based photoreceptor, although it will shift the spectral response towards the long wavelength, it can however lead to unacceptable xerographic performance by, for example, exhibiting fast dark discharge or large residual voltages. By using multilayer photoreceptor structures, the design can be tailored to meet the xerographic specifications. In a typical double-layer photoreceptor of thickness $\sim 60\,\mu$m, the top layer serves as the photogeneration layer (PGL). This layer is only a few micrometres or less in thickness and has a high tellurium content for good panchromatic or red-wavelength absorption. The second layer is called the transport layer (TL) and constitutes the bulk of the photoreceptor through which the photogenerated charge is transported (Fig. 1). In this paper we will be concerned with the fabrication and characterization of single- and double-layer structures only.

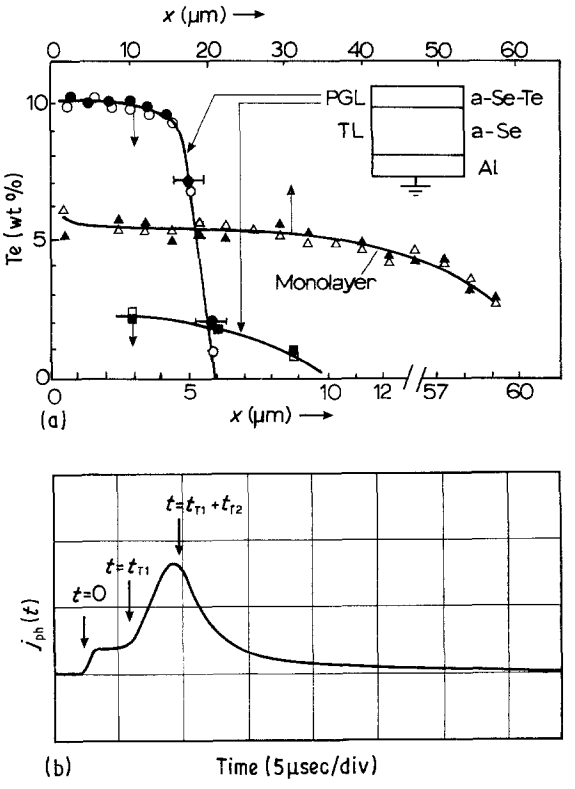

Figure 1 (a) Tellurium concentration against distance x from the surface in typical single- and double-layer photoreceptors (SEM resolution is $\sim 1\,\mu$m). (b) TOF hole photocurrent signal in the double layer a-Se–2.3% Te/Se whose tellurium profile is shown in (a); t_{T1} corresponds to the transit time across the PGL and t_{T2} across the TL [30].

2. Experimental procedure

2.1. Sample preparation and characterization

The xerographic photoreceptors were prepared by vacuum evaporation (10^{-6} to 10^{-5} torr) of vitreous pellets from long stainless steel boats on to heated ($\sim 70°$ C) aluminium substrates as described previously [17]. Various compositions of a-$Se_{1-x}Te_x$ were obtained by mixing the correct amounts by weight of pure selenium with portions of pre-alloyed master batches. The pure selenium pellets used were of xerographic grade, 99.999%, which was confirmed by spark source mass spectrometer analysis.

The stainless steel coating chamber was equipped with a set of independently controlled stainless steel boats and a shutter system to enable the fabrication of multilayer structures. Pure selenium pellets were loaded into one boat and a mixture of selenium and Se:Te pellets in correct amounts into another. The two sources were then evaporated sequentially at boat temperatures of $\sim 300°$ C. Typical coating rates were 1 to 2 μm min^{-1}. The fabrication of xerographic a-$Se_{1-x}Te_x$ films by evaporation techniques has already been widely described and discussed [21–23]. After the evaporation of the selenium alloy, the films were allowed to age or to "anneal" over several months at room temperature during which, via structural bulk relaxation, most physical properties of the photoconductor film become stabilized [24–27]. Differential scanning calorimetric (DSC) studies on the photoreceptor films using a Du Pont Differential Thermal Analyser (Type 990) equipped with the DSC cell showed well-defined glass transition and crystallization peaks as reported previously [17].

Scanning electron microprobe (SEM) analysis on the composition variation across the thickness of a single-layer photoreceptor indicates that due to

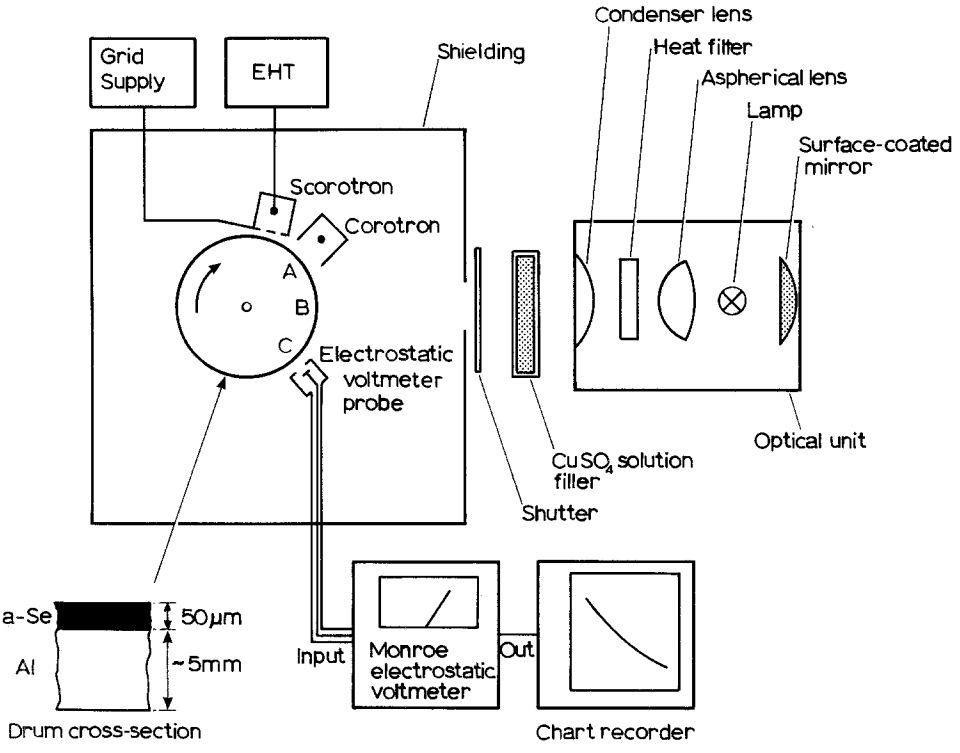

Figure 2 A schematic diagram of the experimental set-up for the measurement of xerographic properties; dark discharge and cycled-up residual voltage.

fractionation effects the top surface was richer in tellurium and the bottom (substrate) region was slightly deficient in tellurium. By shuttering the beginning and the end of the evaporation a reasonably uniform tellurium composition across the film thickness can be obtained. A typical variation in the tellurium concentration across the thickness of a nominal Se–5 wt % Te sample is shown in Fig. 1a. Clearly 5% Te corresponds to the level of tellurium content in the "bulk" of the specimen. The composition of the condensed material at any time during deposition depends on the partial pressures of selenium and tellurium in the vapour. Deviations from Raoult's law will result in condensed layers having different compositions to that of the source. The various bond energies in the a-$Se_{1-x}Te_x$ system are [28] $E_{Se-Se} = 1.91$ eV, $E_{Te-Te} = 1.43$ eV and $E_{Se-Te} = 1.80$ eV; the latter was calculated from the Pauling electronegativity difference $\chi(Se) - \chi(Te) = [E_{Se-Te} - (E_{Se-Se}E_{Te-Te})^{1/2}]^{1/2}$. Because the tellurium atoms in the Se–Te solution are more tightly bound than those in the parent pure tellurium material, their escape tendency is reduced and the tellurium partial pressure is lower than the Raoult value. As a result, the initial stages of the evaporation cause more selenium to be deposited. We wish to bring to attention that excluding the initial and final stages of the coating process, the deposited tellurium content is relatively uniform, as can be seen in Fig. 1a, and close to the starting source value. The kinetics of the evaporation of a-Se–Te alloys will be examined in a future paper.

Fig. 1a also shows tellurium concentration profiles across two typical double-layer photoreceptors whose PGL compositions were nominally 10 and 2.3 wt % Te. Although the SEM analysis has about $\sim 0.5\,\mu m$ resolution it is apparent that the PGL–TL interface in the latter is not as sharp as in the Se–10 wt % Te/Se structure. The nature of the abruptness of the interfaces in multilayer photoreceptor structures and their effect on xerographic performances has not been hitherto studied. Qualitatively a smoother transition will be more desirable, in as much as it will avoid sharp changes in density and will not be expected to lead to a large number of interface defects and traps. Fig. 1b shows an ETOF signal obtained from the Se–2.3% Te/Se double-layer photoreceptor whose profile is that shown in Fig. 1a. The shape of the photocurrent waveform indicates two separate transit times for the two layers [29]. Using appropriate drift mobilities measured on monolayer a-Se–Te alloys, the thickness of the PGL can be estimated. The TOF technique can therefore also be employed as a useful analytical tool to derive information on composition variations across heterogeneous samples, provided that transport data are already available on homogeneous samples [30].

2.2. Xerographic measurements

2.2.1. Dark discharge and saturated residual voltage

Fig. 2 shows a schematic sketch of the experimental set-up used to carry out xerographic discharge and saturated residual voltage experiments. The photoreceptor on a drum was mounted on a rotatable turntable driven by an a.c. motor at the speed corresponding to a period of 1.6 sec. The photoconductor surface was charged by a scorotron or a corotron device. For high initial voltages the output of a high-tension supply was connected to a corotron device, whereas for lower initial voltages (a few hundred volts) the scorotron was used. In the latter case, a potential is applied to a grid placed between the corona charger

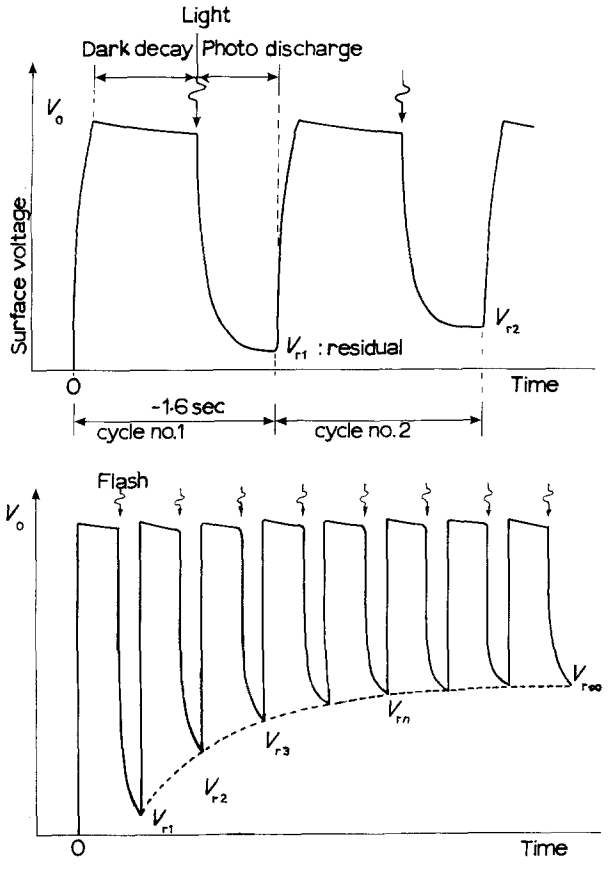

Figure 3 A typical surface voltage against time profile for a photoreceptor during xerographic cycling. The lower figure shows the build-up in the residual voltage as the photoreceptor goes through many xerographic cycles.

and the drum to ensure that the inital voltage on the film does not exceed the required level. The photoreceptor was uniformaly charged by rotating it several times under the corona discharge, after which the latter was switched off. The surface potential was then monitored by a Monroe electrostatic voltmeter (Model 144) with a detector/preamplifier probe (Model 1009A). The photoconductor, the corona charging units and the Monroe voltmeter probe were all housed in a well-shielded and dark environment. The output of the electrostatic voltmeter was connected to a chart recorder which continuously plotted the surface voltage against time.

For saturated residual voltage measurements the charged photoconductor was discharged by a strongly absorbed short-wavelength light through a shutter. The discharge light source was a 250 W 24 V quartz halogen lamp mounted in a projector lamp assembly. A heat filter was used to remove most of the infrared radiation to avoid heating the photoreceptor surface. A $CuSO_4$ solution allowed the filtering of wavelengths longer than ~ 600 nm. Thus the photoconductor was charged at Position A (Fig. 2), discharged at B by an intense blue light and had its residual surface voltage measured at C. This cycle was continuously repeated by rotating the drum until the cycled-up residual voltage reached saturation. Fig. 3a shows the surface potential against time profile in a typical xerographic cycle. Although light discharge occurs very rapidly it leaves behind a residual voltage due to bulk trapped holes. As displayed in Fig. 3b, during the continuous repetition of the xerographic cycle the residual voltage builds up and after many cycles it saturates at $V_{r\infty}$.

A linear version of the above experiment, suitable for xerographic time-of-flight measurements, was also set up. The sample was mounted on a reciprocating platform (schematically sketched in Fig. 4) which transported the specimen horizontally and linearly between the various charging, discharging and detection posts. This system was similar to those described previously by others [18, 31, 32]. The discharge, however, was achieved by an intense xenon flash illumination. The time taken between charging and discharging was about ~ 0.5 sec. The zero of time in dark discharge experiments was taken as the moment of sample arrival under the Monroe electrovoltmeter probe.

2.2.2. Xerographic time-of-flight

Electroded time-of-flight experiments have already been described previously [33, 34] and the XTOF measurements are in principle very similar. They were

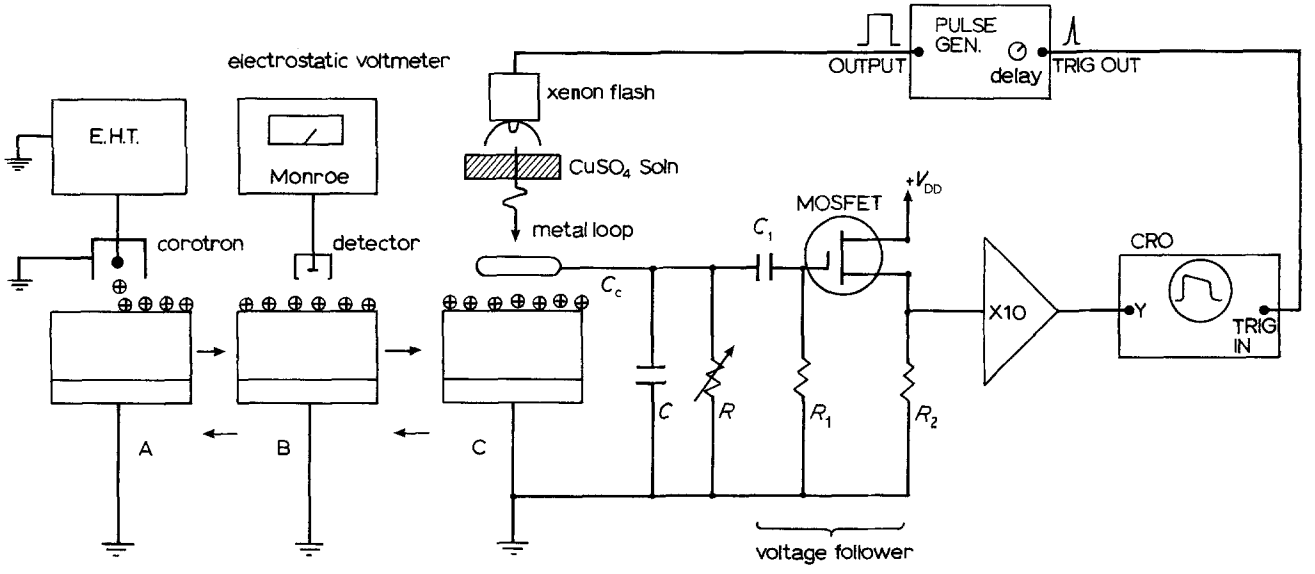

Figure 4 A schematic diagram for XTOF experiments. The apparatus also allowed xerographic dark discharge and cycled-up residual voltage measurements.

carried out by using the experimental arrangement schematically sketched in Fig. 4. The sample is corona-charged at Station A. The surface voltage is measured at B and the XTOF carried out at C. The sample was transported by a reciprocating platform. The apparatus was housed in a well-shielded metallic case. A short low-intensity xenon flash filtered through a $CuSO_4$ solution was used to photogenerate a sheet of holes near the surface of the sample. The photoinjected charge was always much smaller than the surface charge on the sample to maintain small-signal conditions. As the photogenerated charge sheet drifts in the specimen towards the grounded electrode it induces a surface voltage change which is detected by a circular metallic loop positioned above the photoconductor surface and connected to the input of a MOSFET voltage follower. If the time constant RC is much less than any observable transit time t_T in the sample, then the detected signal is proportional to the time derivative of the surface potential on the sample and hence to the photocurrent $j_{ph}(t)$ due to the drift of the photoinjected carriers. In the XTOF configuration the total current, which is the sum of the conduction current and displacement current, must be zero. It can readily be shown that the measured signal is given by

$$V_{sig}(t) = -(RC_C L/\epsilon_0\epsilon_r) j_{ph}(t) \qquad RC \ll t_T \quad (1)$$

and

$$V_{sig}(t) = -(C_C L/C\epsilon_0\epsilon_r) \int_0^t j_{ph}(t)\,dt \qquad RC \gg t_T \quad (2)$$

where C_C is the coupling capacitor between the metallic loop and the sample and C is sample capacitance. The XTOF signals were recorded from the oscilloscope screen by photographing the resulting trace.

3. Results and discussion

3.1. Dark discharge

3.1.1. Pure a-Se

Typical dark discharge results for a pure a-Se film at two different charging voltages are shown in Fig. 5. It is apparent that the decay of the surface potential is relatively slow and has a decreasing time rate, as can be seen from the plots of the time derive dV/dt against t also shown in the same figure. There are a number of physical processes which can lead to the decay of the surface potential. During the corona charging of the photoreceptor, positive ions, $H^+(H_2O)_n$, formed by the corona discharge [35], approach the sample surface and allow electrons from the valence band to tunnel to the ions. This process leaves behind holes which become trapped in deep surface states [36–38]. The measured initial surface voltage is therefore due to deeply trapped holes in surface states. Having identified the nature of the surface charge we can expect the following possible physical mechanisms to cause the dark discharge [39]:

(a) Surface generation and injection of trapped holes and their consequent transport across the sample,

(b) injection from the substrate,

(c) thermal bulk generation of carriers of one sign and depletion.

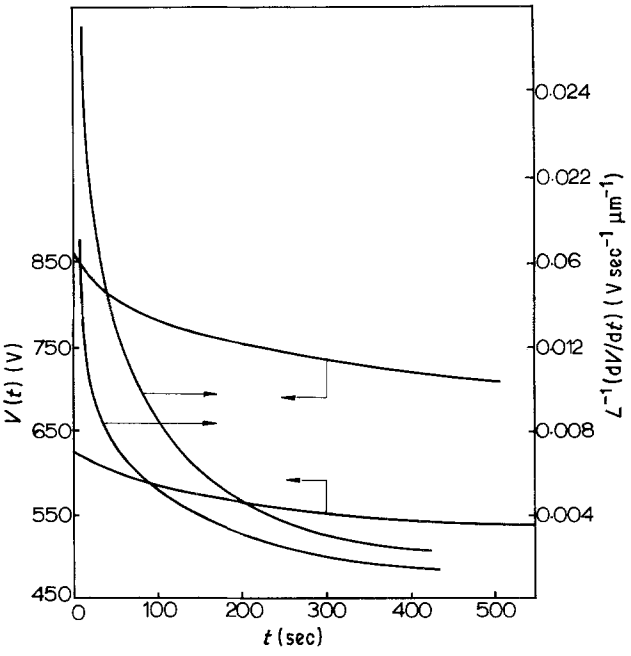

Figure 5 Typical xerographic dark discharge results for pure a-Se showing the time evolution of the surface potential and its time derivative. $L = 49\,\mu m$.

In Case (a) generation from surface states is involved and the rate of surface voltage change is

$$d[V(t)]/dt = -LJ_s(t)/\epsilon_0\epsilon_r \quad (3)$$

where $J_s(t) = d[\varrho_s(t)]/dt$ and $\varrho_s(t)$ is the surface charge per unit area at time t. A similar equation can also be written for Case (b) with J_s replaced by the injection current density J_c from the substrate contact. If the substrate–photoconductor junction is ohmic then $J_c = \sigma V/L$ where σ is the conductivity, and the dark discharge rate is

$$dV/dt = V_0 \exp(-t\sigma/\epsilon_0\epsilon_r) \quad (4)$$

where V_0 is the initial charging voltage and $\sigma/\epsilon_0\epsilon_r$ is the familiar "dielectric relaxation time". Normally the substrate junction is made non-injecting by oxidizing the aluminium substrate surface so that J_c is negligibly small.

In Case (c) bulk thermal generation of holes and their consequent sweep-out leaves a depleted volume of negative ionic centres. The integral of the electric field due to this negative bulk space charge results in a decrease in the measured surface potential. This process has been called the xerographic depletion discharge (XDD) [40, 41]. If $\varrho_n(x, t)$ is the negative space charge density then the rate of change of the surface potential will be given by the time derivative of the double integration of the Poisson equation

$$\frac{d[V(t)]}{dt} = -\frac{1}{\epsilon_0\epsilon_r}\frac{\partial}{\partial t}\int_0^L\int_0^x \varrho_n(x', t)\,dx'\,dx \quad (5)$$

If bulk generation is spatially uniform then Equation 5 is

$$\frac{d[V(t)]}{dt} = -\frac{L^2}{2\epsilon_0\epsilon_r}\frac{d[\varrho_n(t)]}{dt} \quad (6)$$

Thus a general expression for the dark discharge rate will be the sum of Equations 3 and 6 which can be

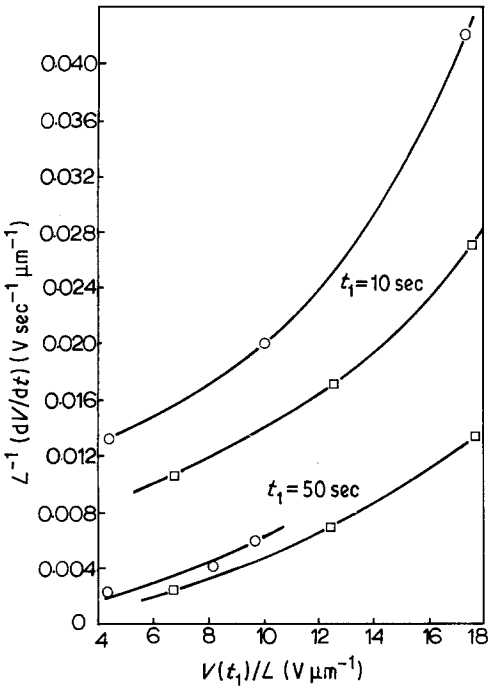

Figure 6 Rate of dark discharge $L^{-1}(dV/dt)$ against $V(t_1)/L$ at fixed times t_1 (10 and 50 sec). (○) L = 67 μm, (□) L = 47 μm.

written in the form

$$\frac{1}{L}\frac{dV}{dt} = \frac{J_{sc}(t)}{\epsilon_0\epsilon_r} + \frac{L}{2\epsilon_0\epsilon_r}\frac{d\varrho_n}{dt} \qquad (7)$$

where $J_{sc} = J_s + J_c$ and is called the surface current. The separation of the dark discharge rate in Fig. 5 into its surface and bulk components is accomplished as follows [42]. From dark discharge rate curves similar to those in Fig. 5, but for different thickness photoreceptors, we can plot $L^{-1}\,dV/dt$ against $V(t_1)/L$ at a fixed time t_1 (e.g. 10 sec) for different values of L as shown in Fig. 6 for two samples. From such curves we can then plot $L^{-1}\,dV/dt$ against thickness L as shown in Fig. 7 at different initial fields $V_0/L \equiv E_0$. We are effectively applying Equation 7 at a fixed time $t = t_1$ to bring out the thickness dependence of $L^{-1}\,dV/dt$. The straight lines in Fig. 7 indicate clearly a bulk generation process for the dark discharge. The intercepts on the $L^{-1}\,dV/dt$ axis, corresponding to $J_{sc}(t_1)/\epsilon_0\epsilon_r$, point to a very small surface component in the dark discharge process.

The slopes of $L^{-1}dV/dt$ against L lines in Fig. 7 represent $(d\varrho_n/dt)/2\epsilon_0\epsilon_r$, which apparently increases with the initial field E_0 as displayed in the inset of Fig. 7 for one discharge time t = 10 sec. The rise in the bulk thermal generation rate with the initial field indicates a field-assisted thermal emission process but with an experimental Poole–Frenkel coefficient β_{exp} about half the theoretical β_{PF} for a-Se. We have found that although β_{exp} for t = 10 sec is about $\frac{1}{2}\beta_{PF}$, for t = 25 and 50 sec, β_{exp} is only ~20% smaller than β_{PF}. It is important to mention that the β_{exp} can only be approximately estimated because the field in the sample is non-uniform. It decreases with time and with distance from the top surface:

$$E(x, t) = E_0 - x\varrho_n(t)/\epsilon_0\epsilon_r \qquad (8)$$

where $E_0 \equiv V_0/L$ is the initial field. As $\varrho_n(t)$ increases with time the average field in the sample $E_{av}(t)$ up to that time decreases, i.e. $E_{av} = bE_0$ where $b(t) < 1$. This means that the slope of the ln $(L^{-1}\,dV/dt)$

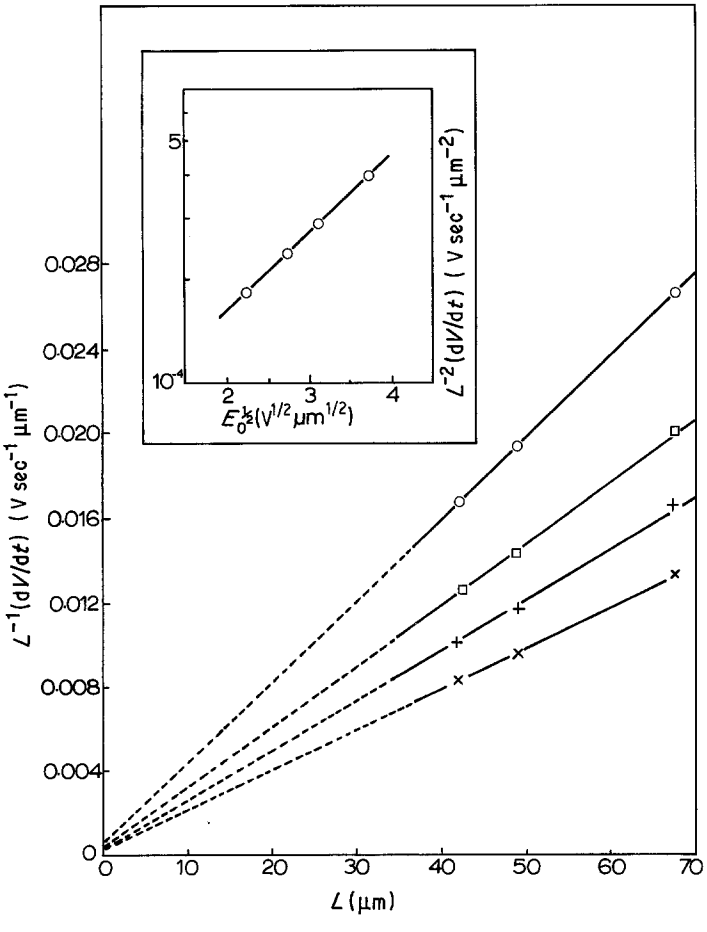

Figure 7 $L^{-1}(dV/dt)$ against L at a fixed time t_1 for different initial fields $E_0 = V_0/L$. Values of E_0 (V μm^{-1}): (x) 5, (+) 7.5, (□) 10, (○) 14. The inset displays $L^{-2}(dV/dt)$ against $E_0^{1/2}$, which indicates the dependence of the bulk thermal generation rate on the initial field.

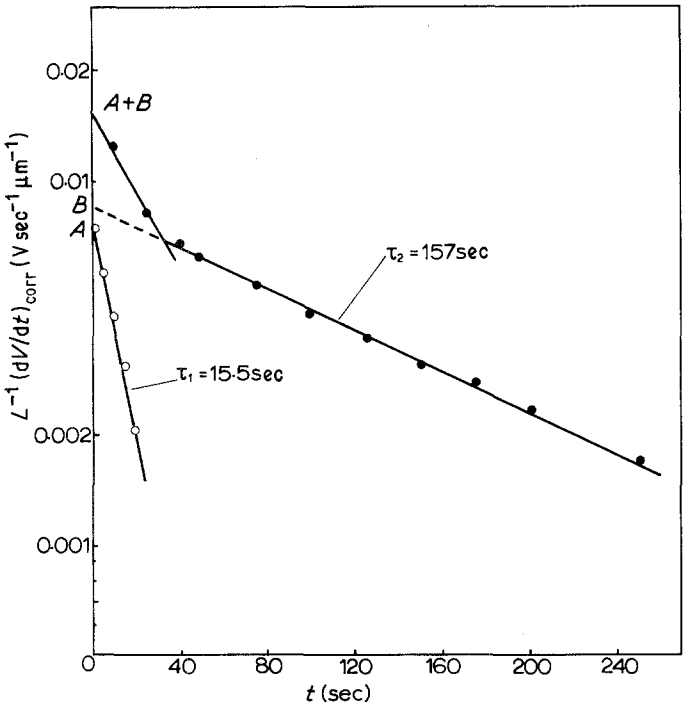

Figure 8 Semilogarithmic plot of the corrected dark discharge rate for bulk generation against time: $L^{-1}V_{cor} = A \exp(-t/\tau_1) + B \exp(-t/\tau_2)$.

against $E_0^{1/2}$ plot (inset of Fig. 7) underestimates the experimental Pool–Frenkel values by at least a factor of $b^{1/2}$. The fact that β_{exp} has been observed to increase with time (but still less than β_{PF}) suggests that two different species of emission centres may be present.

We can subtract the small surface component $J_{sc}/\epsilon_0\epsilon_r$ from the $L^{-1}\,dV/dt$ against t curves in Fig. 5 and plot the corrected discharge rate semilogarithmically against time as in Fig. 8. It can be seen that the dark discharge rate due to bulk generation can be described by

$$L^{-1}\left(\frac{dV}{dt}\right)_{corr} = L\frac{(d\varrho_n/dt)}{2\epsilon_0\epsilon_r} = A\exp\left(\frac{-t}{\tau_{r1}}\right) + B\exp\left(\frac{-t}{\tau_{r2}}\right) \quad (9)$$

with $\tau_{r1} = 15.5$ sec and $\tau_{12} = 157$ sec. Each exponential term represents a set of discrete localized states in the mobility gap from which hole emission occurs, with a probability per unit time

$$\tau_r^{-1} = \nu_0 \exp(-E/kT) \quad (10)$$

where ν_0 is a phonon frequency. Taking $\nu_0 = 1.4 \times 10^{13}\,\text{sec}^{-1}$ [18] we can locate these two states at ~ 0.84 and ~ 0.91 eV above the valence band mobility edge. From physical considerations, the constants A and B are given by

$$A = eLN_1/2\epsilon_0\epsilon_r \qquad B = eLN_2/2\epsilon_0\epsilon_r \quad (11)$$

Substituting the values of A and B from Fig. 8 into Equation 11 we find $N_1 = 1.7 \times 10^{12}\,\text{cm}^{-3}$ and $N_2 = 1.9 \times 10^{13}\,\text{cm}^{-3}$. It can be seen that the dark discharge characteristic of pure a-Se films over the time scales accessed (~ 500 sec) can be explained by a relatively small density of deep mobility gap states from which hole emission occurs.

The initial charging voltage V_0 on a pure a-Se sample under a corotron device with a fixed corona voltage and geometry (e.g. wire to sample distance) was observed to depend strongly on the photoreceptor thickness as shown in Fig. 9. The maximum achievable charging voltage V_0 falls exponentially with the decrease in the thickness L, which is the reason for most commercial photoreceptors having comparable thicknesses (50 to 60 µm). The figure also shows the maximum achievable initial voltages under negative charging. Small negative charge acceptance coupled with only a limited electron transport (discussed later)

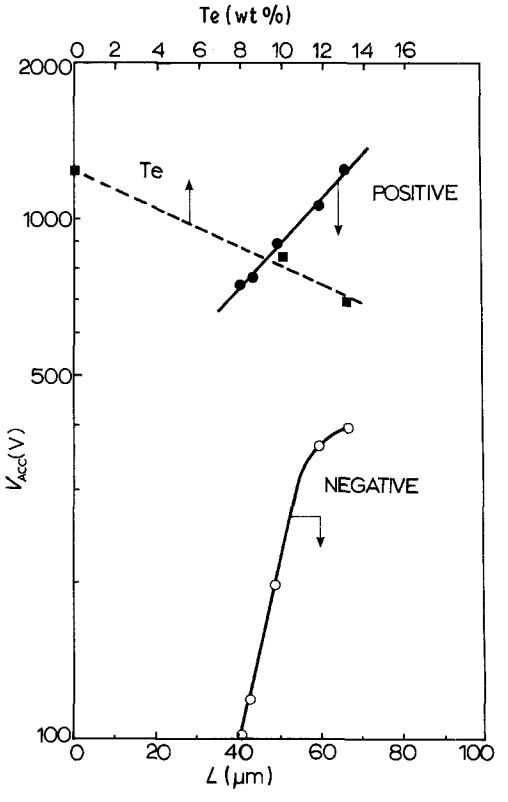

Figure 9 The dependence of the acceptance potential on the thickness for pure a-Se and on the tellurium content for a-$Se_{1-x}Te_x$ alloys. Corona charging conditions and geometry remained unchanged.

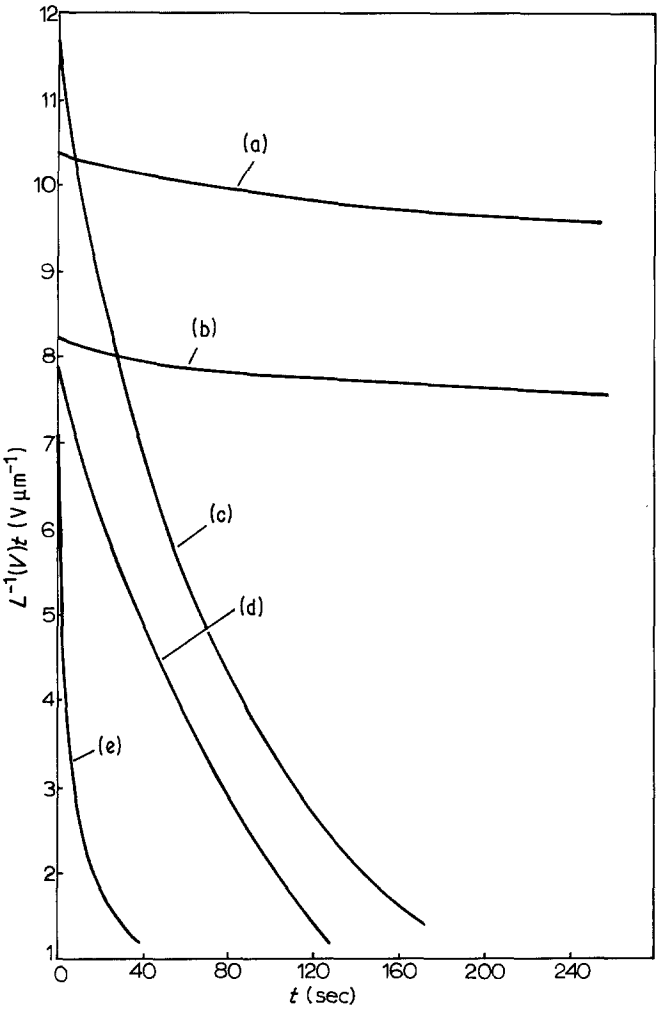

Figure 10 Typical xerographic dark discharge characteristics for (a, c) single- and (b, d) double-layer a-$Se_{1-x}Te_x$-based photoreceptors. (e) shows the effect of chlorine doping on the dark discharge rate. (a) Se–2.7% Te, $L = 15\,\mu m$; (b) Se–2.3% Te/Se, $L_1 = 9.5\,\mu m$, $L_2 = 47.5\,\mu m$; (c) Se–3.5% Te, $L = 65\,\mu m$; (d) Se–10% Te/Se, $L_1 = 6\,\mu m$, $L_2 = 50\,\mu m$; (e) Se + 40 p.p.m. Cl.

preclude the use of a-Se-based photoreceptors under negative charging.

3.1.2. a-$Se_{1-x}Te_x$ alloys

Typical xerographic dark discharge characteristics for single- and double-layer a-$Se_{1-x}Te_x$ photoreceptors are shown in Fig. 10 for the compositions and structures noted in the figure. Comparison of the characteristics for monolayers in Fig. 10 with the dark discharge behaviour of pure a-Se shows clearly that alloying a-Se with tellurium increases the dark decay rate. We can show that the dark discharge rate in a-Se–Te alloys is bulk-controlled by considering the thickness dependence of $L^{-1}\,dV/dt$ at a given time t_1 for a given composition, as shown in Fig. 11 for a-Se with a tellurium content in the range 2.7 to 3.5%. Because of the experimental difficulties involved in fabricating identical composition, homogeneous samples with vastly different thicknesses, the points are not exactly on the line through the origin; but if we make allowances for the variations in the tellurium content then the points would move towards the line, confirming a xerographic depletion discharge model.

Study of Fig. 10 shows that for a double-layer photoreceptor of total thickness 57 μm and PGL composition of 2.3% Te the dark decay (Curve (b)) is much slower than that for a single layer of comparable composition (Curve (c)). This is an advantage of a double-layer structure and also suggests that the dark discharge is due to the Se–Te PGL layer. This is further verified by noting that the dark decay characteristic of the a-Se–2.3% Te/Se double layer (Curve (b)) is similar to that of the single-layer Se–2.7% Te (Curve (a)) of comparable thickness to the PGL. As the tellurium content of the PGL is increased the dark decay becomes faster (Curve (d)).

Fig. 12 shows typical log–log plots of the magnitude of the dark discharge rate dV/dt against time. For the 65 μm thick a-Se–3.5% Te single layer, log $|dV/dt|$ against log t has two linear regions intersecting at what is called a depletion time, t_d. The physical basis for such dark discharge characteristics have been discussed recently in a number of letters by

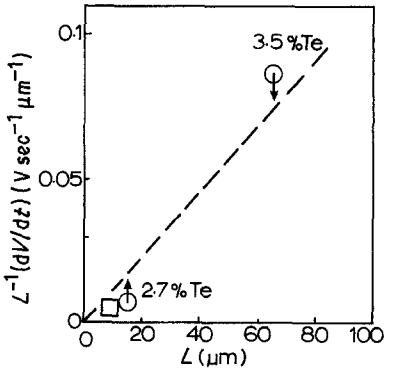

Figure 11 $L^{-1}\,dV/dt$ against L at a fixed time t_1 ($= 40$ sec) less than t_d for a-Se alloyed with ~3 wt % Te; (□) data for the PGL of a-Se–2.3% Te/Se).

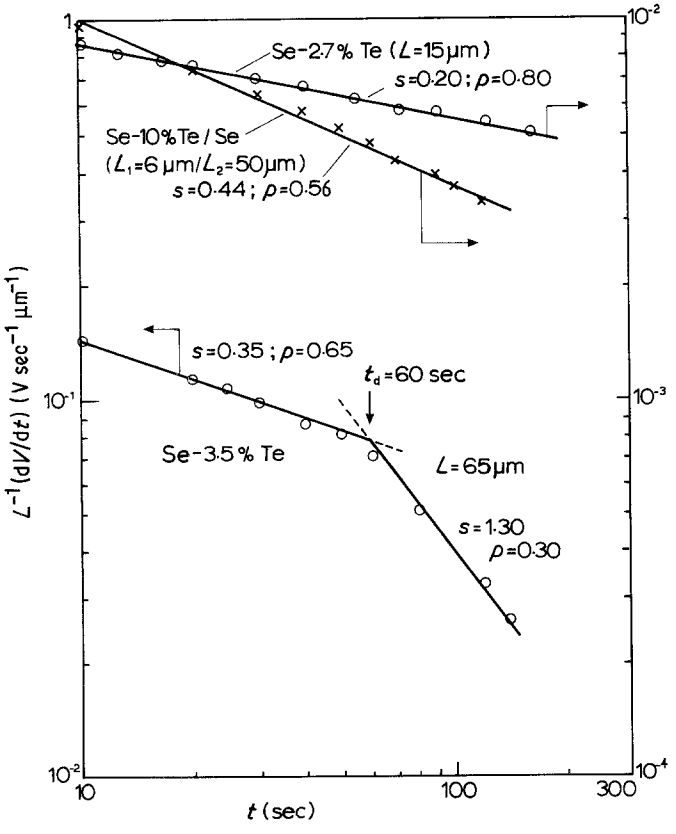

Figure 12 Log–log plots of $L^{-1}\,dV/dt$ against t for single- and double-layer a-$Se_{1-x}Te_x$ photoreceptors.

Xerox workers [43, 44] and the present group [45]. It is believed that the bulk thermal generation of holes in a-Se–Te alloys occurs from deep localized mobility gap states distributed exponentially in energy via a density-of-states function of the form

$$N(\varepsilon) = N_0 \exp|-(\varepsilon - \varepsilon_0)/W| \qquad (12)$$

where the energy ε is measured from ε_{val}, ε_0 is the location of the peak and W is its energy "width". The xerographic depletion discharge model then predicts [41] that $\varrho_n(t)$ in the sample increases with time as t^p where $p \equiv kT/W$, and as a consequence the dark discharge rate is

$$dV/dt \sim t^{-(1-p)} \qquad t < t_d \qquad (13)$$

$$dV/dt \sim t^{-(1+p)} \qquad t > t_d \qquad (14)$$

where the depletion time t_d, is the time when the field at the grounded substrate end of the sample is zero. From Equation 8, t_d is given by $E(L, t_d) = 0$, i.e. when $\varrho_n(t_d) = \epsilon_0\epsilon_r V_0/L^2$. This is the reason for not observing a depletion time over the experimental time scale for thin samples in Fig. 12. We have found the parameter p to decrease monotonically with the tellurium content (Fig. 12) , which indicates that tellurium addition broadens the energy distribution of the deep localized states.

The dependence of the maximum initial charging voltage V_0 on the content is shown in Fig. 9. As tellurium is added to a-Se, V_0 falls nearly linearly with the tellurium content. Although tellurium alloying of a-Se decreases the number of surface atoms per unit area n_s, by virtue of a reduction in the atomic bulk concentration n_b, the fractional decrease in n_s is much smaller than that in V_0 for a given corotron voltage and geometry [46].

3.1.3. Chlorine-doped a-Se

Chlorine in small amounts (e.g. 10 to 40 wt p.p.m.) is sometimes added to a-Se and its a-Se–As and a-Se–Te alloys to improve the xerographic residual voltage. As shown in Fig. 10, the dark discharge with 40 wt p.p.m. Cl doping of a-Se is so rapid that as a photoreceptor this system has no practical usefulness. The effect of introducing chlorine into the Se–Te alloys will not be reported in this paper. The dark decay curve for a-Se + 40 wt p.p.m. Cl is included in Fig. 10 to show the general effect of chlorine doping.

3.2. Saturated residual voltage

3.2.1. Pure a-Se

During the continuous repetition of the xerographic cycle on a pure a-Se film, the residual voltage V_{rn} at cycle number n was found to evince the typical behaviour shown in Fig. 13. The rate of increase in V_{rn} with n decreases as cycling increases, until eventually for large n ($\geqslant 100$) V_{rn} tends to a saturated value $V_{r\infty}$ which

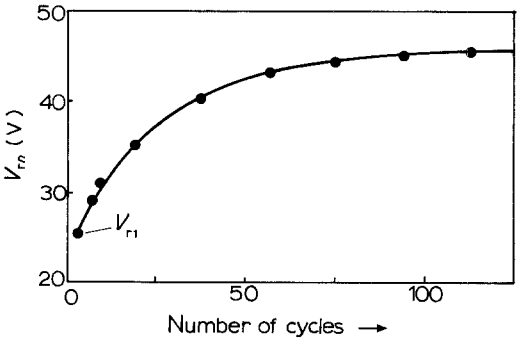

Figure 13 The build-up in the residual voltage with the number of xerographic cycles. V_{r1} is the first-cycle residual voltage. (The charging voltage $V_0 \approx 620$ V).

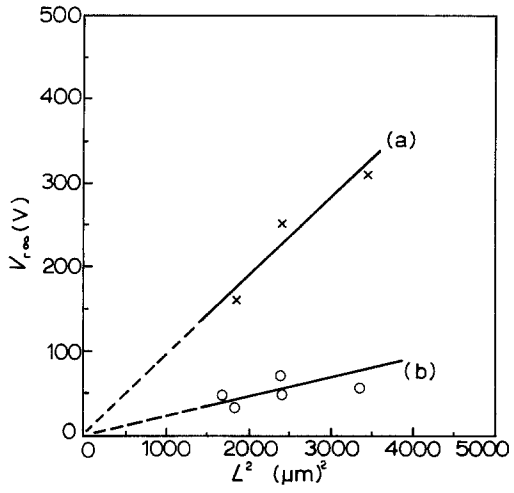

Figure 14 Saturated residual voltage against L^2 for (a) freshly prepared a-Se films ($N_t = 7.08 \times 10^{13}\,cm^{-3}$) (b) well aged (>3 months) a-Se films ($N_t = 1.73 \times 10^{13}\,cm^{-3}$).

for the particular sample in Fig. 13 is ~45 V. It was observed that lengthening the cycle period from 1.6 to 3.5 sec had no effect on the saturated residual voltage.

Provided that after a sufficient number of cycles all the deep traps have been filled, the saturated residual voltage $V_{r\infty}$ will be given by

$$V_{r\infty} = eL^2N_t/2\epsilon_0\epsilon_r \qquad (15)$$

where N_t is the density of deep traps, assumed to be uniformly distributed in the sample. Fig. 14 shows a plot of $V_{r\infty}$ against L^2 for freshly prepared a-Se films aged for less than 7 days (Fig. 14a) and for well-annealed films aged for at least 3 months (Fig. 14b). The slope of the straight line drawn to pass through the origin and the experimental points was used to calculate the concentration N_t of deep traps. As noted in Fig. 14, N_t in well-annealed and rested samples is $\sim 1.7 \times 10^{13}\,cm^{-3}$. This value is very close to the density of deep centres, $\sim 1.9 \times 10^{13}\,cm^{-3}$, from which hole emission occurs (see Section 3.1.1.). It is possible that dark discharge and residual voltage build-up involve essentially the same species of localized centres. For example, dark decay may involve the ionization of a neutral defect centre D^0, perhaps corresponding to Se_3^0, via $D^0 \rightarrow D^- + h^+$ where D^- represents an undercoordinated selenium atom, Se_1^-. On the other hand the residual voltage may depend on $D^0 + h^+ \rightarrow D^+$ where D^+ represents an overcoordinated selenium atom, Se_3^+. If this is the case, then the concentration of D^0 centres is $\sim 2 \times 10^{13}\,cm^{-3}$, and less than that required for the absence of an ESR signal [47, 48]. It is also possible that we may be observing amphoteric behaviour by intimate valence alternation pairs, IVAPs ([49, 50]; [51] and references therein). An IVAP comprises over and under-coordinated selenium atoms Se_3^+ and Se_1^- in close proximity, behaving as if it were a "neutral" centre. The capture of a hole by Se_1^- exposes the positive charge on Se_3^+ and explains the residual voltage detected. The emission of a hole from the Se_3^+ uncovers the negative charge on Se_1^- which causes the dark decay.

Saturated residual voltage is an important comparative xerographic parameter which depends on the distribution and nature of traps. In general if $\varrho_t(x)$ represents the spatial distribution of charge in deep traps in a sample which has no dielectric discontinuity (which excludes multilayers), then the measured residual will be

$$V_r = (\epsilon_0\epsilon_r)^{-1} \int_0^L \int_0^x \varrho_n(x')\,dx'\,dx \qquad (16)$$

For $\varrho_t = eN_t$ leads to Equation 15.

3.2.2. a-$Se_{1-x}Te_x$ alloys

The effect of tellurium addition to a-Se on the saturated residual voltage $V_{r\infty}$ is shown in Fig. 15a. $V_{r\infty}$ initially increases with the tellurium concentration to nearly three to four times that for pure a-Se, and beyond 6 to 8 wt % Te $V_{r\infty}$ begins to fall. At ~17 wt % Te, $V_{r\infty}$ is only slightly higher than in the a-Se case. The density of deep hole traps N_t, calculated from Equation 15 with the appropriate relative

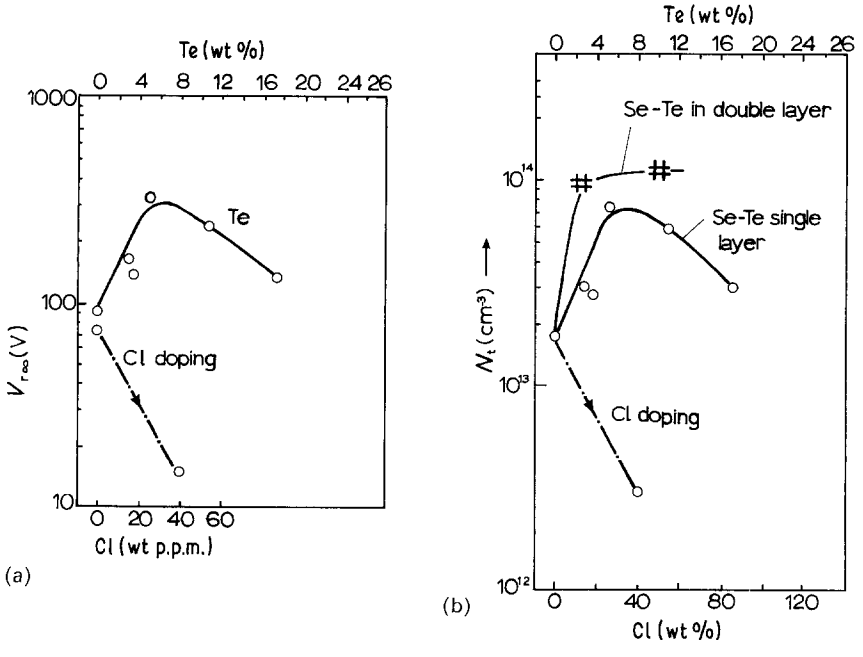

Figure 15 (a) The dependence of the saturated residual voltage $V_{r\infty}$ on the tellurium content and chlorine doping for comparable thickness samples (L = 56 to 63 μm). (b) Deep hole trap density N_t against tellurium content and chlorine doping: (○) in monolayer photoreceptors, (#) in the PGL of a-Se–Te/Se.

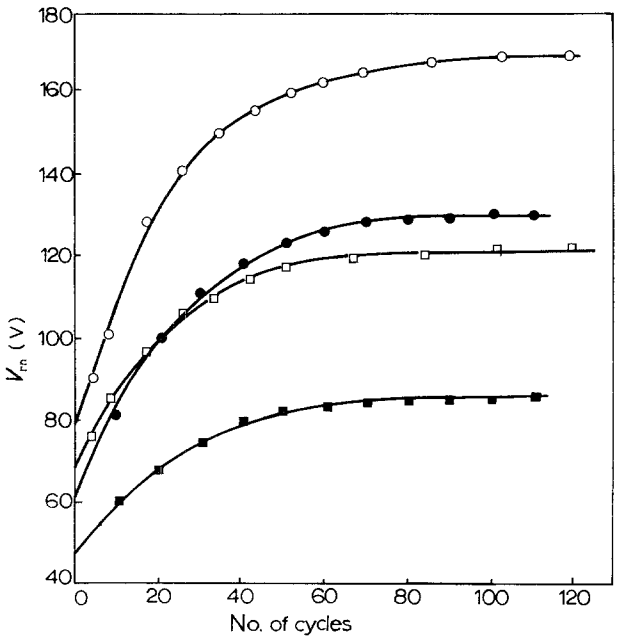

Figure 16 Cycling of the residual voltage V_{rn} in a-Se–Te/Se double layers. The filled points refer to the PGL obtained by subtracting the contribution from the a-Se TL. (○) Se–2.3% Te/Se, (●) PGL (L = 9.5 μm); (□) Se–10% Te/Se, (■) PGL (L = 6 μm).

permittivity (see Fig. 17b below), follows a similar behaviour with the tellurium content as shown in Fig. 5(b). There may be various reasons for the fall in $V_{r\infty}$ with the tellurium content beyond ~7 wt %. Firstly, because of monotonic decrease in the band-gap with the tellurium composition, the release time τ_r from deep traps may not remain sufficiently long in comparison to the cycle time to allow an eventual saturation of the deep traps. As more tellurium is added, τ_r becomes shorter and a small fraction of N_t gets filled; hence the fall in $V_{r\infty}$. Another aspect is that, owing to rapid bulk thermal generation of holes and their sweep-out during the time between charging and discharging, there will be a volume density of negative centres. Recombination of a photoinjected hole with a negative ion will convert the latter to a neutral site and hence will not result in a detectable surface potential. The neutral states responsible for the observed residual voltage may be of IVAP type ([51] and references therein) or may be true neutral defect centres of the type C_3^0 or C_1^0, where C is a selenium or tellurium atom.

Fig. 16 shows the build-up of the residual voltage in two double-layer photorecepts whose PGLs have the tellurium compositions indicated. To obtain the residual voltage due to the PGL alone we must subtract from V_{rn} against n the data for homogeneous pure a-Se layers (Fig. 13). When this is carried out we obtain the V_{rn} against n behaviour displayed by the filled points in Fig. 16. Although the saturated residual voltages are now due to the PGLs we still cannot use Equation 15 directly to calculate the density of deep traps in the PGL, in as much as Equation 15 is valid for a single homogeneous layer. We need to solve the Poisson equation for the double-layer heterogeneous structure in Fig. 17a which includes a dielectric mismatch at $x = L_2$. The following boundary conditions must be satisfied for a complete solution:

(i) $V = 0$ at $x = 0$.
(ii) $E = 0$ at $x = L_2 + L_1$.
(iii) $\epsilon_{r1} E_1 = \epsilon_{r2} E_2$ at the interface; $x = L_2$.
(iv) $V(x)$ is continuous throughout.

The saturated residual is then given by $V_{r\infty} = V(L_1 + L_2)$, i.e.

$$V_{r\infty} = \frac{eN_{t2}L_2^2}{2\epsilon_0\epsilon_{r2}} + \frac{eN_{t1}[L_1^2 + 2L_1L_2(\epsilon_{r1}/\epsilon_{r2})]}{2\epsilon_0\epsilon_{r1}} \quad (17)$$

where the subscripts 1 and 2 refer to the PGL and TL. The saturated residual due to the PGL alone is therefore given by

$$V_{r\infty}(\text{PGL}) = \frac{eN_{t1}[L_1^2 + 2L_1L_2(\epsilon_{r1}/\epsilon_{r2})]}{2\epsilon_0\epsilon_{r1}} \quad (18)$$

which depends not only on L_1^2 but also on L_1L_2 as well as on both the dielectric constants. To calculate N_{t1} from Equation 18 we need the variation in the relative permittivity ϵ_{r1} with the tellurium content. Fig. 17b shows the dependence of ϵ_r on the tellurium concentration from capacitance measurements. Application of Equation 18 to the $V_{r\infty}$ data in Fig. 16 leads to the density of deep traps in the PGL as a function of tellurium content as shown in Fig. 15b. It seems that the density of deep traps in the PGL is larger than that expected from measurements on single layers. The difference may be due to the presence of deep hole traps at the interface between the PGL and the TL where there is a sharp variation in the material density. We may make a tentative estimate for the number

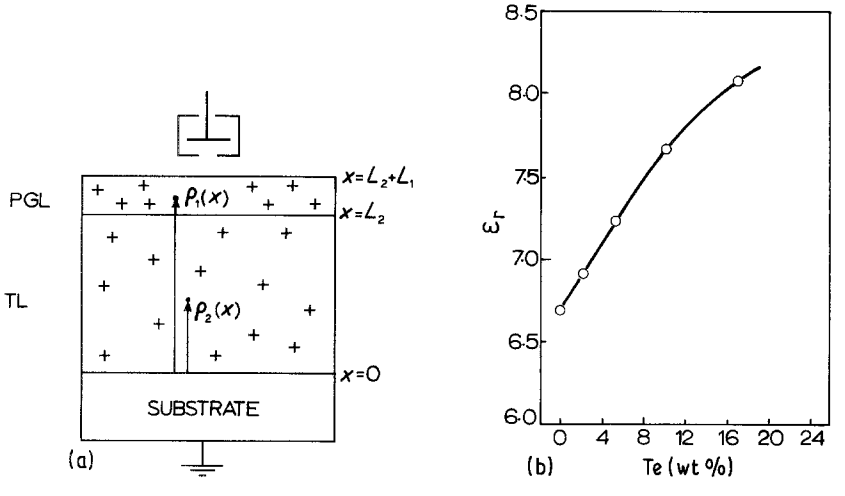

Figure 17 (a) Analysis of the residual voltage in double layer photoreceptors. Trapped charge densities ϱ_1 and ϱ_2 in the PGL and TL are different. (b) The dependence of the dielectric constant on the tellurium concentration in a-Se–Te alloys.

of unmatched atoms at this interface by calculating the number of atoms per unit area on either side of the interface via $n_s = n_b^{2/3}$, where n_s and n_b are the surface and bulk atomic concentrations and $n_b = N_A d/M_r$; d is the density, N_A the Avogadro number and M_r the relative atomic mass. For the Se–10% Te/Se structure the atomic mismatch (Δn_s) is $\sim 10^{13}$ atoms cm^{-2} which translates to an effective bulk concentration ($\Delta n_s/L_1$) of $\sim 10^{16}$ cm^{-3} possible traps in the PGL when interpreted via the saturated residual voltage measurement. Although the mismatch effect was calculated for a step junction, it does however imply that the density variation across the interface is more than sufficient to account for larger concentrations of deep traps observed in the PGL than in the case of single layers of a-Se–Te. In addition to highly strained bonds in the interface region, we would also expect that, in view of the large atomic mismatch, some of the selenium chains will be terminated at the interface by an Se_1^- type of defect which of course can act as a hole trap.

3.2.3. Chlorine-doped a-Se

The saturated residual voltage in 40 wt p.p.m. Cl doped a-Se was found to be markedly reduced as shown in Fig. 15a. This implies a decrease in the concentration of deep hole traps N_t with chlorine introduction into a-Se (Fig. 15b). Previous time-of-flight experiments on chlorine-doped a-Se samples showed an enhancement of the hole lifetime τ_h as measured from the shape of the transient photocurrent waveform [23, 34] which is in general agreement since $\tau_h \sim 1/N_t$. It is interesting to note that although there is a reduction in the number of deep hole traps, the fast dark discharge (Fig. 10) exhibited by a-Se + Cl indicates a large increase in the concentration of hole emission centres near the middle of the mobility gap.

3.3. Time-of-flight measurements

Both XTOF and TOF experiments were carried out on a-$Se_{1-x}Te_x$ alloys to determine the change in the nature of hole and electron transport with the addition of tellurium. The results of the TOF measurements were recently reported by the present authors [16].

Fig. 18 displays a typical transient hole photocurrent waveform $j_{ph}(t)$ from TOF measurements on a pure a-Se sample. The decay in the waveform before the transit time has been in the past [23–34, 52, 53] used to determine the hole lifetime τ_h by plotting $\log j_{ph}$ ($t < t_T$) against time t as shown in Fig. 18. This assumes that the photoinjected holes reach thermal equilibrium with the shallow traps very quickly (over a time $\ll t_T$) and that trapping during the transit involves deep traps with release times $\tau_r \gg t_T$. The semilogarithmic plots of $j_{ph}(t)$ against t in Fig. 8 indicate that for undoped a-Se, $\tau_h \approx 9.4\,\mu$sec. We can check this interpretation by evaluating τ_h through the first-cycle residual voltage V_{r1}. From Fig. 13 when $V_0 = 620$ V, the first-cycle residual $V_{r1} = 23$ V so that $v_r \equiv V_{r1}/V_0 = 0.037$. Using the universal $V_r = V_r/V_0$ against τ/t_r curve of Kanazawa and Batra (Fig. 1 in [54]) we find $\tau_h \approx 12\,\mu$sec, which is close to that from the TOF measurement.

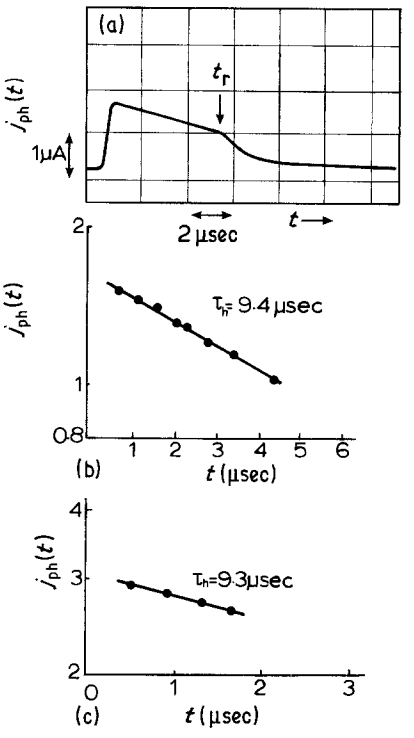

Figure 18 (a) A typical oscilloscope trace of the TOF photocurrent hole signal in a-Se; 40 V, $L = 58\,\mu$m. (b, c) Semilogarithmic plots of the magnitude of the photocurrent against time ($< t_T$) at two different voltages: (b) ETOF, 40 V, $\tau_h = 9.4\,\mu$sec; (c) XTOF, 115 V, $\tau_h = 9.3\,\mu$sec.

Since both τ_h and the first-cycle residual V_{r1} are due to the same species of deep traps whose concentration from $V_{r\infty}$ is $\sim 1.7 \times 10^{13}$ cm^{-3} we can evaluate the capture coefficient $C_t = \sigma_c v_c$ where σ_c is the capture cross-section and v_c is the free carrier velocity near the mobility edge E_v (in crystalline semiconductors v_c is the thermal velocity). The range, $\mu_h \tau_h$, in shallow-trapped controlled transport is given by [55, 56].

$$\mu_h \tau_h = \mu_o \tau_{ho} = \mu_o/(N_t C_t) \qquad (19)$$

where μ_0 is the microscopic mobility and τ_{ho} is the hole lifetime in the absence of shallow traps ($\tau_{ho} = 1/N_t C_t$). Substituting $\mu_o \approx 0.39$ cm^2 V^{-1} sec^{-1} [33], $\mu_h = 0.16$ cm^2 V^{-1} sec^{-1}, $\tau_h \approx 0.4\,\mu$sec and $N_t \approx 1.7 \times 10^{13}$ cm^{-3} in Equation 19 we find $C_t \approx 1.2 \times 10^{-8}$ cm^3 sec^{-1}. Taking $v_c = v_{th} = 10^7$ cm sec^{-1} leads to a capture cross section $\sigma_c \approx 1.2 \times 10^{-15}$ cm^2 and a capture radius $r_c \approx 0.2$ nm. These values suggest hole trapping by neutral centres either of D^0 type or IVAP. The actual capture cross-section is probably larger than that estimated, in as much as v_c may not be equal to the thermal velocity [57]. It is interesting to compare σ_c for hole capture in a-Se with $\sigma_c \approx 2 \times 10^{-15}$ cm^{-2} for hole capture by neutral centres in a-Si–H [58, 59].

With the addition of tellurium both the hole and electron drift mobility, μ_h and μ_e, fall in magnitude and also exhibit a weak algebraic field dependence of the form $\mu \propto E^n$ as shown in Fig. 19. The index n is larger for the electron mobility, and increases in both cases with the tellurium content. The inset of Fig. 19 shows the behaviour of μ_h and μ_e with the tellurium concentration. The fall in μ_e with tellurium addition is more rapid than for μ_h.

Saturated residual voltage measurements indicated

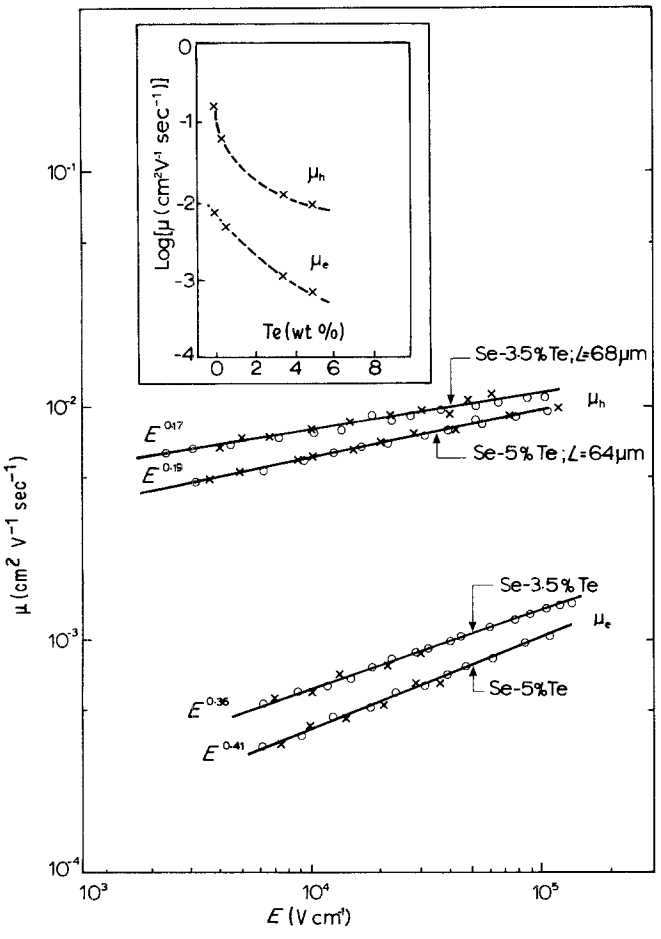

Figure 19 Electric field dependence of the hole and electron drift mobility in a-Se–Te alloys from (x) XTOF and (○) ETOF measurements. The inset shows the decrease in the hole and electron drift mobilities with the tellurium concentration.

an increase in the density of deep traps. The excess photocurrent hole lifetime from Equation 19 is

$$\tau_h = \mu_o/\mu_h N_t C_t \qquad (20)$$

For a-Se–5% Te, $\mu_h \approx 6 \times 10^{-3}\,cm^2\,V^{-1}\,sec^{-1}$ (a typical value over the fields accessed; Fig. 19), $N_t \approx 7 \times 10^{13}\,cm^{-3}$ (Fig. 15b) with μ_o and C_t assumed unchanged leads to a τ_h value of $\sim 60\,\mu sec$. Had there not been an increase in τ_h is would not have been possible to observe hole photocurrents in a-Se–Te alloys because the typical transit times $t_T = L^2/\mu_h V$ are much longer than τ_h in pure a-Se, implying a trap-limited transport. The enhanced photocurrent hole lifetime is due to a tellurium induced increase in the density of shallow traps. The factor which reduces the drift mobility acts to enhance the excess hole lifetime as stated in Equation 19.

4. Conclusions

Xerographic dark discharge experiments on a-Se photoreceptors indicate that the decay of the surface potential over the time-scale of observation (~ 500 sec) is essentially due to bulk thermal generation of holes, their consequent sweep-out and depletion. XTOF experiments carried out by Xerox workers [19, 20] have confirmed a build-up of negative bulk space charge during dark discharge. Hole emission occurs from discrete midgap localized states and it is field-assisted.

When a-Se is alloyed with tellurium the dark discharge becomes more rapid. It is still controlled by a bulk thermal generation process, $dV/dt \sim L^2$, but both the volume density and energy spread of the midgap localized states increase with the tellurium content. In double-layer photoreceptors of the type a-Se–Te/Se (minimum tellurium content 2.3 wt %), although the thickness of the PGL layer was nearly a factor of ten smaller than the TL, the dark discharge was mainly due to the tellurium-rich PGL. The charge acceptance of a-$Se_{1-x}Te_x$ alloys was found to fall with the tellurium composition.

The repetition of the xerographic cycle over many cycles leads to the saturation of the surface residual voltage which was used to determine the density N_t of deep hole traps. The deep hole trap concentration in a-Se was calculated to be $\sim 1.9 \times 10^{13}\,cm^{-3}$ and was comparable to that for the hole emission centres. This suggests that the two species of localized states may be identical in origin, perhaps an IVAP acting as a "neutral" centre. The saturated residual voltage increases with the tellurium content in a-$Se_{1-x}Te_x$ up to ~ 7 wt % due to tellurium-introduced deep traps. The analysis of the saturated voltage in a-Se–Te/Se layers leads to larger densities of deep hole traps in the PGL than if the PGL were a single layer. The difference was attributed to the presence of deep hole traps at the PGL–TL interface where there is a change in the atomic concentration.

The XTOF measurements on a-$Se_{1-x}Te_x$ films confirm the earlier results from the electroded TOF experiments [16] that both the hole and the electron drift mobility μ_h and μ_e decrease with the tellurium content, the effect on the latter being stronger. The reduction in the hole mobility can be explained by an increase in tellurium-introduced shallow traps. Combining the TOF data with N_t from the saturated residual voltage experiments gives a capture

coefficient C_t of $\sim 1.2 \times 10^{-8}$ cm^3 sec^{-1} for pure a-Se, indicative of "neutral" trapping sizes.

Chlorine doping of a-Se up to 40 wt p.p.m. resulted in very rapid dark discharge and a fall in the saturated residual voltage.

It can be seen that in a-$Se_{1-x}Te_x$ alloy photoreceptors, the improvements achieved in thermal and mechanical properties [60] and the increase in the spectral sensitivity towards the red are accompanied by an accelerated xerographic dark discharge and larger residual voltages due to tellurium-introduced deep and shallow hole traps.

Acknowledgements

We wish to thank Mr J. R. Hardwick of Gestetner Byfleet Ltd, Surrey, England, for financial support, and Dr R. Rollason (also of Gestetner Byfleet Ltd) and Mr M. Baxendale of this group for many useful discussions.

References

1. B. E. SPRINGETT, in Proceedings of the 3rd International Symposium on Industrial Uses of Selenium and Tellurium Stockholm, Sweden, 1984 (Selenium–Tellurium Development Association, Darien, USA) pp. 285–295.
2. W. J. MURPHY, in Proceedings of the 3rd International Symposium on Industrial Uses of Selenium and Tellurium Stockholm, Sweden, 1984 (Selenium–Tellurium Development Association, Darien, USA) pp. 279–285.
3. I. CHEUNG, G. M. T. FOLEY, P. FOURNIA and B. E. SPRINGETT, *Phtogr. Sci. Engng* **26** (1982) 245.
4. K. TATEISHI and Y. HOSHINO, *IEEE Trans. Elec. Dev.* **ED-31** (1984) 793.
5. K. KIYOTA, A. TESHIMA and M. TANAKA, *Photogr. Sci. Engng* **24** (1980) 289.
6. A. R. MELNYK, J. S. BERKES and L. B. SCHEIN, in Proceedings of the First International Congress on Advances in Non-Impact Printing Technologies for Computer and Office Applications, Venice, 1981, edited by J. Gaynor (Van Nostrand Reinhold, New York, 1982) pp. 503–509.
7. Y. TANIGUCHI, H. YAMAMOTO, S. HORIGOME, S. SAITO and E. MARUYAMA, *J. Appl. Phys.* **52** (1981) 7261.
8. J. H. HEYHART, *Photogr. Sci. Engng* **10** (1966) 126.
9. H. ADACHI and K. C. KAO, *J. Appl. Phys.* **51** (1980) 6326.
10. A. L. DAWAR, J. C. JOSHI and L. NARAIN, *Thin Solid Films* **76** (1981) 113.
11. S. H. HAGEN and P. J. A. DERKS, *J. Non-Cryst. Solids* **65** (1984) 241.
12. J. C. SCHOTMILLER, M. TABAK, G. LUCOUSKY and A. WARD, *ibid.* **4** (1970) 80.
13. T. TAKAHASHI, *ibid.* **34** (1979) 312.
14. M. ABKOWITZ and J. M. MARKOWICS, *Solid State Commun.* **44** (1982) 1431.
15. S. O. KASAP and C. JUHASZ, *J. Non-Cryst. Solids* **72** (1985) 23.
16. C. JUHASZ, M. VAEZI-NEJAD and S. O. KASAP, *J. Imaging Sci.* **29** (1985) 144.
17. S. O. KASAP and C. JUHASZ, *J. Mater. Sci.* **21** (1986) 1329.
18. M. ABKOWITZ and R. C. ENCK, *Phys. Rev.* **B25** (1982) 2567.
19. S. B. BERGER and R. C. ENCK, in Proceedings of the International Symposium on Industrial Uses of Selenium and Tellurium, Toronto, 1980 (Selenium–Tellurium Development Association, Darien, USA) p. 197.
20. S. B. BERGER, R. C. ENCK, M. E. SCHARFE and B. E. SPRINGETT, in "Physics of Selenium and Tellurium", edited by E. Gerlach and P. Grosse (Springer, New York, 1979) p. 256.
21. J. S. BERKES, in Proceedings of Second International Conference on Electrophotography, Washington, DC, 1974, edited by D. R. White (Society of Photographic Scientists and Engineers, Springfield, Virginia, USA, 1974) p. 137.
22. J. C. SCHOTTMILLER, *J. Vac. Sci. Technol.* **12** (1975) 807.
23. M. D. TABAK and W. J. HILLEGAS, *ibid.* **9** (1972) 387.
24. G. C. DAS, M. B. BEVER, D. R. UHLMANN and S. C. MOSS, *J. Non-Cryst. Solids* **7** (1972) 251.
25. R. B. STEPHENS, *ibid.* **20** (1976) 75.
26. M. ABKOWITZ, *Polym. Eng. Sci.* **24** (1984) 1149.
27. *Idem. J. Non-Cryst. Solids* **77/78** (1984) 1191.
28. L. PAULING, "The Nature of the Chemical Bond", 3rd Edn. (Cornell University Press, Ithaca, 1968) pp. 60 and 64.
29. Y. OKAMOTO and K. NAKAMURA, *Electrophotography (Japan)* **17** (1979) 26.
30. S. M. VAEZI-NAJAD and C. JUHASZ, *Thin Solid Films* in press.
31. M. ABKOWITZ and R. C. ENCK, *Phys. Rev.* **B27** (1983) 7402.
32. A. W. ING and J. H. NEYHART, *J. Appl. Phys.* **43** (1972) 2670.
33. S. O. KASAP and C. JUHASZ, *J. Phys. D* **18** (1985) 703.
34. *Idem, Photogr. Sci. Engng* **26** (1982) 239.
35. M. M. SHAHIN, *J. Chem. Phys.* **45** (1967) 2600.
36. D. W. VANCE, *J. Appl. Phys.* **42** (1971) 5430.
37. P. K. WATSON, in Proceedings of 5th Conference on Electrostatic Phenomena, Oxford, England, 1979, edited by J. Cowell (Conference Series No. 48) (Institute of Physics, Bristol, England, 1979) p.1.
38. H. KLESS, *RCA Rev.* **30** (1975) 667.
39. M. SCHARFE, "Electrophotography Principles and Optimisation" (Research Studies Press, Letchworth, England, 1984) Ch. 4.
40. A. MELYNK, *J. Non-Cryst. Solids* **35/36** (1980) 837.
41. M. ABKOWITZ, F. JANSEN and A. R. MELNYK, *Phil. Mag.* **B51** (1985) 405.
42. L. B. SCHEIN, *Phys. Rev.* **10** (1974) 3451.
43. M. ABKOWITZ, G. M. T. FOLEY, J. M. MARKOWICS and A. C. PALUMBO, *Appl. Phys. Lett.* **46** (1985) 393.
44. M. ABKOWITZ, G. M. T. FOLEY, J. M. MARKOWICS and A. C. PALUMBO, in Proceedings of Conference on Optical Effects in Amorphous Semiconductors, Snowbird, Utah, 1984, edited by P. C. Taylor and S. G. Bishop (AIP Conference Proceedings No. 120) (American Institute of Physics, New York, 1984) p. 117.
45. C. JUHASZ, S. O. KASAP and M. BAXENDALE, to be published.
46. R. M. SCHAFFERT, "Electrophotography" (Focal Press, London, 1975) pp. 237–247.
47. M. ABKOWITZ, *J. Chem. Phys.* **46** (1967) 4537.
48. S. C. AGARWAL, *Phys. Rev.* **B7** (1973) 685.
49. M. KASTNER, D. ADLER and H. FRITZSCHE, *Phys. Rev. Lett.* **37** (1976) 1504.
50. P. ADLER and E. YOFFA, *Can. J. Chem.* **55** (1977) 1920.
51. M. KASTNER, *J. Non-Cryst. Solids* **31** (1978) 223.
52. M. TABAK and P. J. WARTER, *Phys. Rev.* **173** (1968) 899.
53. W. HERMS, H. KARSTEN and U. ZERRENTHIN, *Phys. Status Solidi (a)* **23** (1974) 479.
54. K. K. KANAZAWA and I. P. BATRA, *J. Appl. Phys.* **43** (1972) 1845.
55. R. M. BLAKNEY and H. P. GRUNWALD, *Phys. Rev.* **159** (1967) 658.
56. I. P. BATRA and H. SEKI, *J. Appl. Phys.* **41** (1970) 3409.
57. R. A. STREET, *Phil. Mag.* **49** (1984) L15.
58. *Idem. Appl. Phys. Lett.* **41** (1982) 1060.
59. R. A. STREET, J. ZESCH and M. J. THOMPSON, *ibid.* **43** (1983) 672.
60. C. JUHASZ and S. O. KASAP, *J. Mater. Sci. Lett.* in press.

Received 27 August
and accepted 9 October 1986